Catalysis
Science &
Technology

PAPER

View Article Online
View Journal

Cite this: DOI: 10.1039/c4cy01461h

Catalytic oxidation of formaldehyde over manganese oxides with different crystal structures†

Jianghao Zhang, Yaobin Li, Lian Wang, Changbin Zhang* and Hong He

Received 7th November 2014,
Accepted 17th January 2015

DOI: 10.1039/c4cy01461h

www.rsc.org/catalysis

α-, β-, γ- and δ-MnO_2 catalysts were prepared by a hydrothermal method and tested for the catalytic oxidation of formaldehyde (HCHO) at low temperature. Dramatic differences in activities among the MnO_2 catalysts with different crystal structures were observed. The δ-MnO_2 catalyst exhibited the best activity among the four catalysts and achieved nearly complete HCHO conversion at 80 °C, while the α-, β- and γ-type MnO_2 obtained 100% HCHO conversion at 125 °C, 200 °C, 150 °C, respectively. The catalysts were next characterized by Brunauer–Emmett–Teller (BET), X-ray diffraction (XRD), Field-Emission Scanning Electron Microscopy (FE-SEM), temperature-programmed reduction by H_2 (H_2-TPR), X-ray photoelectron spectroscopy (XPS) and temperature-programmed desorption of HCHO (HCHO-TPD) methods to investigate the factors influencing the catalytic activity. Based on the characterization results, it is supposed that the tunnel structure and active lattice oxygen species are the main factors that contribute to the excellent performance of δ-MnO_2. According to the high catalytic performance and facile preparation process, δ-MnO_2 may potentially be used as a support in applications of supported catalysts.

1. Introduction

Formaldehyde (HCHO) emitted from widely used building and decorative materials has become the main indoor air pollutant in airtight houses.[1] Exposure to HCHO may cause several of the following syndromes: eye, nose or throat irritation; coughing; fatigue and severe allergic reactions, *etc.*[2,3] According to the latest study, HCHO is also harmful to the nervous system and cardiovascular system.[4] Hence, effective abatement of indoor air HCHO is urgently needed in order to improve air quality and reduce the public health risk.

Several approaches for HCHO removal have been studied during decades of research, including photo-catalytic oxidation,[5,6] plasma decomposition with catalyst,[7] adsorption[8] and catalytic oxidation.[9–11] However, photo-catalytic oxidation needs light containing ultraviolet wavelengths to excite the catalyst, and may lead to the formation of harmful by-products. Plasma technology has significant limitations such as the poor performance under low concentrations of HCHO and possible harmful by-products such as ozone.[2] The effectiveness of adsorption materials is limited by the maximum capacity and the hazard of desorption during regeneration. The catalytic oxidation method spurns the above drawbacks and could selectively decompose low concentration toxic HCHO to harmless CO_2 and H_2O even at ambient temperature. It has been shown to be a promising method for indoor air HCHO removal.[12]

There are two main kinds of catalysts for HCHO oxidation including supported noble metal (Pt, Au, Rh and Pd)[13–18] and non-noble metal oxide (Ag, Co, Ce and Mn)[10,19–24] catalysts. The supported noble metal catalysts such as alkali-metal-doped Na–Pt/TiO_2,[9,25] Pt/MnO_x–CeO_2,[16] TiO_2 supported Pd nanoparticles,[17] and Na-promoted Pd/TiO_2,[18] have shown remarkable catalytic activities at ambient temperature even at high space velocity. However, the high price inhibited their wide application. In contrast, the transition metal oxides are much cheaper; some catalysts have also proven to be effective for low temperature HCHO oxidation. Therefore, the transition metal oxides are regarded as promising alternative catalysts to noble metal catalysts.

Mn based catalysts have been widely studied for HCHO oxidation and appear to be the most active catalysts among the transition metal oxides. It was reported that the preparation method, morphology, tunnel structures, *etc.*, have considerable influence on the catalytic activity of Mn based catalysts. Tang *et al.* reported that MnO_x–CeO_2 prepared by a modified co-precipitation method showed a better performance than those prepared with sol–gel or co-precipitation methods, achieving complete HCHO conversion at 373 K.[26]

State Key Joint Laboratory of Environment Simulation and Pollution Control, Research Center for Eco-Environmental Sciences, Chinese Academy of Sciences, 18 Shuangqing Road, Beijing 100085, China. E-mail: cbzhang@rcees.ac.cn; Fax: (+86) 10 62849121; Tel: (+86) 10 62849121

† Electronic supplementary information (ESI) available. See DOI: 10.1039/c4cy01461h

Chen *et al.* found that MnO_x with a hollow nanostructure had a much higher activity than that with a honeycomb nanostructure.[27] Chen *et al.* studied the tunnel structure effect on Mn oxide activity and suggested that the [2 × 2] tunnel structure could dramatically elevate the catalytic activity of Mn oxides.[28] Wang *et al.* observed that the 3D ordered cubic mesoporous Co–Mn oxide is a highly effective catalyst for HCHO oxidation and obtained the complete oxidation of HCHO at 70 °C.[29]

In this study, MnO_2 catalysts with α-, β-, γ- and δ-phase structures were prepared by a hydrothermal process and then tested for their performance in the catalytic oxidation of formaldehyde (HCHO) at low temperature. A dramatic difference in the catalytic activity was clearly observed between the four kinds of MnO_2. δ-MnO_2 showed the best catalytic activity of the four materials, achieving almost 100% conversion of 170 ppm HCHO at 80 °C with a gas hourly space velocity of 100 000 mL $(g_{cat}\ h)^{-1}$. The catalysts were carefully characterized by XRD, BET, FE-SEM, H_2-TPR, XPS and HCHO-TPD measurements. Based on the results, the factors affecting the catalytic activity were elucidated.

2. Experimental section

2.1 Preparation of catalysts

The four kinds of manganese oxide with different phase structures were prepared by a hydrothermal method according to the previous report.[30] For the α-MnO_2, 0.525 g $MnSO_4 \cdot H_2O$ and 1.25 g $KMnO_4$ were mixed in 80 mL distilled water, then stirred magnetically for about 30 min to form a homogeneous solution before it was moved into a Teflon-lined stainless steel autoclave (100 mL). After that, the autoclave was heated to 160 °C for 12 h in an oven. The product was collected, washed, filtered, dried at 80 °C and then calcined at 300 °C. The procedures for the preparation of other manganese oxides were similar to that of α-MnO_2 except for the precursor, the reaction temperature and the reaction duration.

For β-MnO_2, 1.69 g $MnSO_4 \cdot H_2O$ and 2.28 g $(NH_4)_2S_2O_8$ reacted at 140 °C for 12 h.

For γ-MnO_2, 3.375 g $MnSO_4 \cdot H_2O$ and 4.575 g $(NH_4)_2S_2O_8$ reacted at 90 °C for 24 h.

For δ-MnO_2, 0.275 g $MnSO_4 \cdot H_2O$ and 1.5 g $KMnO_4$ were heated to 240 °C for 24 h.

2.2 Characterization

The structure parameters, pore characterization and specific surface area of the samples were obtained by a BET plot using a Quantachrome Quadrasorb SI-MP at −196 °C over the whole range of relative pressures. The pore size distribution was calculated by the desorption branch of the N_2 adsorption isotherm using the BJH method. Before the N_2 physisorption, the catalysts were degassed at 300 °C for 5 h.

XRD patterns were measured on an X'Pert PRO MPD X-ray powder diffractometer with Cu Kα radiation operated at 40 kV and 40 mA. The 2θ angle ranged from 10° to 80° with a scan step of 0.02°.

Field-Emission Scanning Electron Microscopy (FE-SEM) images were obtained using an SU-8020 scanning electron microscope. The samples for FE-SEM measurements were prepared by depositing the powder on a conductive tape using N_2 vertical purging. The voltage exerted for lower amplification was 3 kV while for higher amplification was 1 kV.

Temperature-programmed reduction (TPR) was carried out on a Chemisorption Analyzer (AutoChem 2920) equipped with a TCD detector. After sweeping by Ar and air successively, a flow of 10% H_2/Ar at a rate of 50 $cm^3\ min^{-1}$ (STP) passed the samples with the temperature increasing from 100 to 600 °C at a rate of 10 °C min^{-1}. The H_2 consumption was monitored by TCD after produced H_2O removal.

X-ray photoelectron spectroscopy (XPS) profiles were obtained by an AXIS Ultra system, equipped with Al Kα radiation ($h\nu$ = 1486.6 eV) with an anode operated at 225 W and 15 kV. The binding energy values were calibrated using the C 1s peak (284.8 eV). The surface relative composition was estimated from the integrated intensities corrected by atomic sensitivity factors.

The temperature-programmed desorption of HCHO (HCHO-TPD) measurements on the samples were carried out on a Micromeritics AutoChem II 2920 instrument. The catalysts were loaded in a quartz reactor and heated at 200 °C for 0.5 h in the argon flow to remove the absorbed CO_2 and H_2O. After being cooled to −20 °C, the samples were saturated by HCHO–helium mixed gas for 1 h. Then the flow gas was changed to pure helium for 0.5 h, followed by temperature ramping to 250 °C at a linear rate of 10 °C min^{-1}. The products HCHO and CO_2 were monitored using a Cirrus II Mass Spectrometer at m/z ratios of 30 and 44, respectively.

2.3 Activity test

The activity tests for the catalytic oxidation of HCHO over the catalysts (60 mg) were performed in a fixed-bed quartz flow reactor (i.d. = 4 mm) in an incubator. Gaseous HCHO was generated by flowing nitrogen through the paraformaldehyde container in a water bath kept at 35 °C. The feed gas composition was 170 ppm HCHO, 20% O_2 and 25% RH balanced by N_2. The total flow rate was 100 mL min^{-1}, corresponding to a gas hourly space velocity (GHSV) of 100 000 mL $(g_{cat}\ h)^{-1}$. δ-MnO_2 was also tested under a high GHSV of 600 000 mL $(g_{cat}\ h)^{-1}$ to control HCHO conversion below 100% for the measurement of specific reaction rate.

As with our previous activity evaluating instruments and methods,[9,18] the inlet and outlet gases were monitored by FTIR spectroscopy (Nicolet iS50) equipped with 2 m gas cell and a DTGS detector; resolution: 0.5 cm^{-1}; OPD velocity: 0.4747 cm s^{-1}. The collection region was 4000–600 cm^{-1} and the number of scans per spectrum was 16. HCHO and CO_2 were measured by the peaks located at 2897 (C–H vibration) and 2350 cm^{-1} (O–C–O vibration), respectively. Since no other carbon containing compounds except for CO_2 were detected in the effluents for all tested catalysts, the HCHO and CO_2 concentrations were quantified and calculated based on the peak area of CO_2 at 2350 cm^{-1}.

The lattice oxygen test experiments were also carried out over δ-MnO_2 to check the role of the lattice oxygen species in the HCHO oxidation reaction. The initial HCHO concentration, catalyst amount and GHSV were the same as the normal activity test experiment. In detail, the procedure is as follows: the samples were first pretreated at 150 °C for 30 min in a flow of pure O_2 at a rate of 20 mL min^{-1}. Then the purging gas was switched to pure N_2 at a rate of 100 mL min^{-1} for 30 min to remove gaseous O_2 and the weakly absorbed oxygen species. After that, the temperature was lowered to X °C (X = 50, 75) and then the HCHO balanced with N_2 was introduced into the reactor and the products were monitored by FTIR spectroscopy.

3. Results and discussion

3.1 Crystal structure and morphology of catalyst

XRD patterns were measured to investigate the crystallographic structures of the samples and the results are shown in Fig. 1. All of the four samples could be well indexed and were in good agreement with the lattice constants of α-MnO_2 (JCPDS 44-0141), β-MnO_2 (JCPDS 24-0735), γ-MnO_2 (JCPDS 14-0644) and δ-MnO_2 (JCPDS 80-1098), confirming the successful preparation of MnO_2 with four types of crystal structures, which were also verified by the Raman spectra and lattice distances measured by high-resolution transmission electron microscopy (HR-TEM) (ESI,† Fig. S1 and S2). In addition, it could be inferred that α-MnO_2 and β-MnO_2 had high crystallinity according to their narrow peak widths and high intensities. In contrast, γ-MnO_2 presented a very poor XRD pattern. As reported, γ-MnO_2 is normally the product of irregular intergrowth of elements of ramsdellite and pyrolusite,[31,32] thus no complete single crystal will emerge in the structure, leading to the low crystallinity of γ-MnO_2. δ-MnO_2 generally has the disordered structures in certain crystallographic directions.[33] Therefore, δ-MnO_2 showed much broader and weaker XRD peaks than those of α-MnO_2 and β-MnO_2.

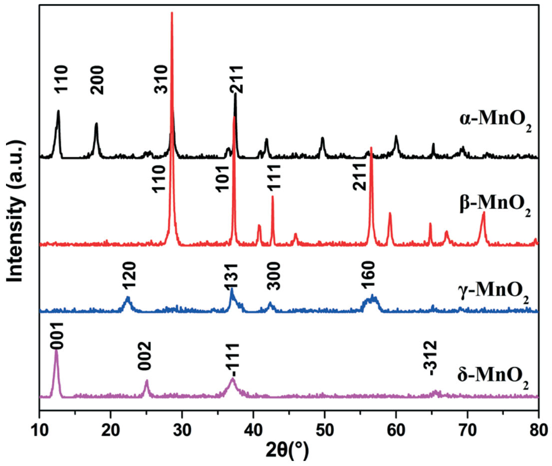

Fig. 1 XRD patterns of α-, β-, γ- and δ-MnO_2 samples.

Table 1 shows the specific surface areas (S_{BET}), average pore sizes (d), and total pore volumes (V) of the four samples. δ-MnO_2 showed the highest S_{BET}, average pore size (d) and V among the four catalysts. The α- and γ-MnO_2 samples exhibited much similar moderate values of S_{BET}, d and V. In contrast, β-MnO_2 presented the lowest parameters.

FE-SEM images of the α-, β-, γ- and δ-MnO_2 samples (two magnifications for each) are shown in Fig. 2. α-MnO_2 showed a dendritic nanostructure (Fig. 2a) which was composed of uniform nanorods; the size of each individual nanorod is about 2.5 μm long and 30 nm wide. β-MnO_2 had similar dendritic nanostructures (Fig. 2b) which consisted of tetragonal prism nanorods, 2 μm long and 50–100 nm wide. γ-MnO_2 displayed a spherical nanostructure which was composed of MnO_2 nanoneedles with sharp tips. The γ-MnO_2 nanoneedles had lengths of about 2.5 μm and diameters of about 40 nm. δ-MnO_2 also had a spherical morphology with a diameter of 2–3 μm, which was built up of many interleaving nanoflakes composed of very thin nanowires with widths of 10–20 nm. The morphology of the samples was also surveyed by HRTEM (ESI,† Fig. S2), which showed consistent results with the SEM images.

3.2 Activity test

Fig. 3 shows the HCHO conversion to CO_2 as a function of temperature over the α-, β-, γ- and δ-MnO_2 catalysts at a GHSV of 100 000 mL $(g_{cat}\ h)^{-1}$ with an inlet HCHO concentration of 170 ppm. The temperature dependence of the HCHO conversions were distinctly related to the phase structures of MnO_2. The catalytic activities followed the sequence δ- > α- > γ- > β-MnO_2. δ-MnO_2 showed the best catalytic activity among the four samples and 100% HCHO conversion was obtained at around 80 °C. The other catalysts α-, β- and γ-MnO_2 exhibited a much lower activity than δ-MnO_2 with 100% HCHO conversions achieved at 125 °C, 200 °C, and 150 °C, respectively. The above findings clearly showed that the catalytic activity of MnO_2 for the oxidation of HCHO was in tight correlation with the crystal structures. In order to eliminate the influence of surface area, the specific reaction rate (R_s) at 100 °C in terms of the generated amount of CO_2 per

Table 1 Specific surface area (S_{BET}), average pore size (d), total pore volume (V) and normalized reaction rate (R_s) of the α-, β-, γ- and δ-MnO_2 catalysts

Samples	S_{BET} [m^2 g^{-1}]	Pore diameter (d) [nm]	Pore volume (V) [cm^3 g^{-1}]	R_s [nmol s^{-1} m^{-2}]
α-MnO_2	80.8	13.2	0.27	1.87
β-MnO_2	23.3	11.4	0.05	0.63
γ-MnO_2	85.3	12.2	0.26	0.44
δ-MnO_2	108.4	14.1	0.38	9.42

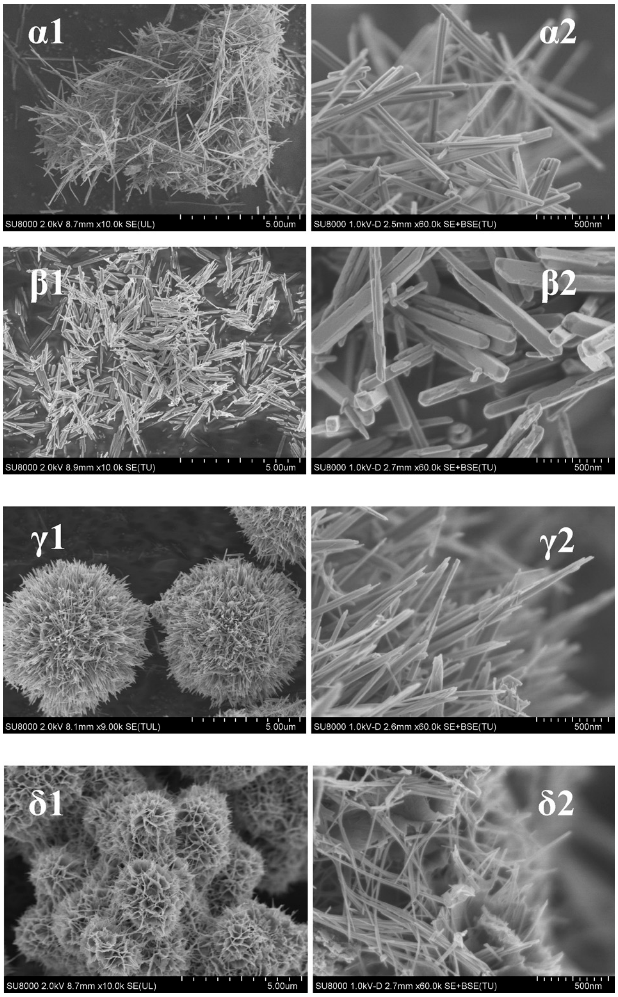

Fig. 2 SEM images of the α-, β-, γ- and δ-MnO_2 samples, 1 and 2 refer to different magnifications of one sample.

unit area is calculated and given in Table 1. For the R_s measurement, δ-MnO_2 was tested under a high GHSV of 600 000 mL $(g_{cat}\ h)^{-1}$ with a conversion of 80.5% at 100 °C. As shown in Table 1, the R_s of δ-MnO_2 is 9.42 nmol s^{-1} m^{-2}, which is much higher (around 5 times that of the second best) than the other catalysts. These results indicate that the oxidation of HCHO is drastically enhanced on the δ-MnO_2 catalysts, implying δ-MnO_2 could be a potential catalyst for HCHO oxidation. Liang *et al.*[30] have tested the catalytic properties of α-, β-, γ- and δ-MnO_2 catalysts for CO oxidation. They observed that the catalytic activities decreased in the order α- ≈ δ- > γ- > β-MnO_2 and the α-MnO_2 catalyst had a similar activity to δ-MnO_2. However, in this study, the series of catalysts showed a different catalytic behaviour for HCHO oxidation and δ-MnO_2 was much more active than α-MnO_2. Therefore, the key factor affecting the activity of the MnO_2 catalysts should be different for these two reactions.

The stability of the δ-MnO_2 catalyst was checked by long isothermal tests at 75 °C with a GHSV of 150 000 mL $(g_{cat}\ h)^{-1}$. As shown in Fig. 4, in the beginning, there is a certain rise of the conversion rate which might be due to some highly active and non-renewable adsorbed oxygen species. The rate then dropped and stabilized at around 60%. Overall, the sample exhibited excellent stability and efficiency, and the approximately 60% HCHO conversion rate was maintained over a 30 h-long test. After the reaction and stability tests, the XRD patterns of the four catalysts were also measured, and the results showed that their crystalline structures remained intact (ESI,† Fig. S3).

3.3 Effect of K^+

There are several factors that might influence the activity of manganese oxides. Hou *et al.*[34] have reported that increasing the K^+ content would drastically enhance the catalytic activity of OMS-2 catalysts for the catalytic oxidation of benzene.

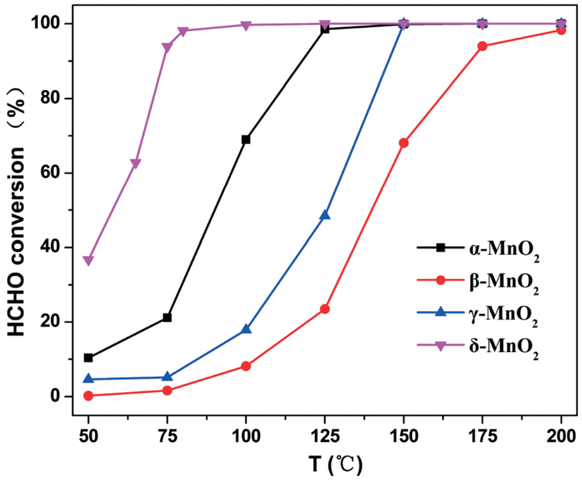

Fig. 3 HCHO conversions over α-, β-, γ- and δ-MnO_2 samples. Reaction conditions: 170 ppm of HCHO, 20% O_2, N_2 balance, GHSV = 100 000 mL $(g_{cat}\ h)^{-1}$.

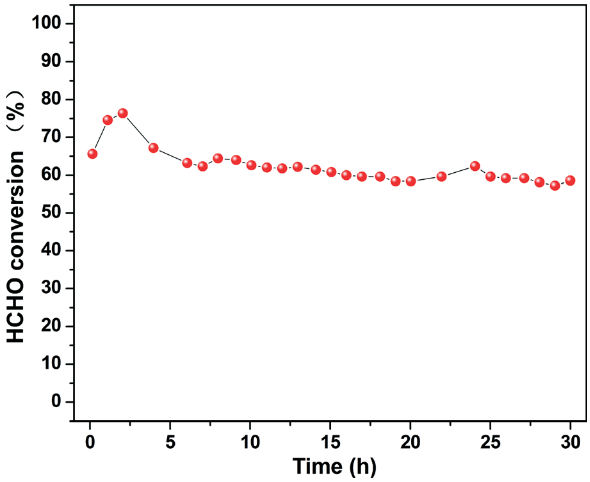

Fig. 4 Stability test of the δ-MnO_2 catalyst in terms of the production amount of CO_2. Reaction conditions: 75 °C, 170 ppm of HCHO, 20% O_2, N_2 balance, GHSV = 150 000 mL $(g_{cat}\ h)^{-1}$.

Therefore, we first investigated the possible effect of the K^+ species on the catalytic activity of the series of MnO_2 catalysts for HCHO oxidation. ICP-OES was carried out to measure the K^+ content in the four catalysts and the quantitative results are summarized in Table 2. The K^+ volume in α-MnO_2 and δ-MnO_2 was 7.1 wt.% and 6.4 wt.%, respectively, and no K^+ was detected in the β- and γ-MnO_2 catalysts. The amount of K^+ in α-MnO_2 (7.1 wt.%) was slightly higher than that in δ-MnO_2 (6.4 wt.%), however, α-MnO_2 showed a much lower activity for HCHO oxidation than δ-MnO_2, indicating that the K^+ presence was not the reason for the activity difference between these two catalysts. α-MnO_2 without K^+ species was next prepared following the procedures reported by Hou *et al.*[34] and then tested under the same conditions as the normal activity test. An activity comparison of the two kinds of α-MnO_2 sample as well as the γ- MnO_2 sample is shown in Fig. 5. It is indicated that the activity of α-MnO_2 slightly dropped in the absence of K^+ species, but is still much higher than γ-MnO_2. Thus, it could be concluded that the K^+ species was not the main factor affecting the activities of the four types of MnO_2 catalyst for HCHO oxidation.

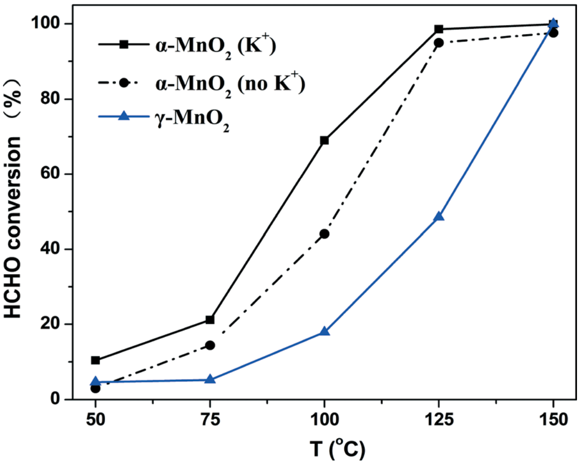

Fig. 5 Activity test of the three samples: α- with/without K^+ and γ-MnO_2. Reaction conditions: 170 ppm of HCHO, 20% O_2, N_2 balance, GHSV = 100 000 mL $(g_{cat}\ h)^{-1}$.

3.4 Tunnel structure

As reported, the four kinds of MnO_2 catalyst contain different types of tunnel structures.[35] α-MnO_2 consists of [2 × 2] and [1 × 1] tunnel structures. β-MnO_2 is composed of a [1 × 1] tunnel structure. γ-MnO_2 contains both [1 × 1] and [1 × 2] tunnels. In contrast, δ-MnO_2 forms a 2D layer structure. Therefore, the distinction in activities between the MnO_2 catalysts might be partially ascribed to the different tunnel structures. Liang *et al.*[30] have reported that the tunnel structure could affect the CO chemisorption, therefore obviously influence the catalytic activity of MnO_2 for CO oxidation. In addition, Chen *et al.*[28] have observed that MnO_2 with the [2 × 2] tunnel structure is much more active than MnO_2 with the [1 × 1] or [3 × 3] structure for HCHO oxidation since the effective diameter of the [2 × 2] tunnel is more suitable for the HCHO diffusion during the reaction. Our results were consistent with the reported result in that α- was more active than β- and γ-. Moreover, the present results also suggested that the interlayer structure of MnO_2 would benefit the HCHO oxidation reaction more than the [2 × 2] tunnel structure by facilitating the absorption and diffusion of HCHO molecules to active sites. Therefore, the different tunnel structure among α-, β-, γ- and δ-MnO_2 catalysts should be one of the reasons for their different activities.

3.5 Reducibility of catalyst

H_2-TPR experiments were next performed to investigate the reducibility of the four samples. Fig. 6 shows the H_2-TPR profiles of the α-, β-, γ- and δ-MnO_2 catalysts. β-MnO_2 presented a sharp peak at 301 °C with a broad peak at 419 °C. Accounting for the peak area which could indicate the hydrogen consumption amount, the ratio of the lower temperature peak to the higher one is about 2 : 1. This is a typical feature of the reduction of MnO_2, consistent with conversion of MnO_2 to Mn_3O_4, which leads to the lower temperature peak, and then Mn_3O_4 to MnO leading to the higher temperature one.[34] The pattern of γ-MnO_2 with the location of peaks at 305 °C and 403 °C exhibited a certain similarity with that of β-MnO_2, and shows that the same reduction processes occurred as for β-MnO_2. In contrast, α-MnO_2 exhibited two reduction peaks at 292 °C and 319 °C. Similarly, δ-MnO_2 also showed two overlapping reduction peaks located at 269 °C and 285 °C. However, the ratio of the lower temperature peak to the higher temperature peak was about 1 : 1, which may indicate the existence of a different reduction route, that is MnO_2 to Mn_2O_3 and then to MnO. Nevertheless, it is clear from these results that the reduction capacity sequence should be δ- > α- > γ- ≈ β-, which is consistent with the previous report.[30]

Table 2 The K^+ content determined by ICP-OES and the XPS data for the α-, β-, γ- and δ-MnO_2 samples

Samples	K^+ content [wt%]	Binding energy [eV]		Molecular ratio	Binding energy [eV]		Molecular ratio
		Mn^{4+}	Mn^{3+}	Mn^{4+}/Mn^{3+}	O_{latt}	O_{ads}	O_{latt}/O_{ads}
α-MnO_2	7.1	642.6	641.8	5.6	529.7	531.3	4.1
β-MnO_2	0	642.2	641.5	4.2	529.3	530.8	2.4
γ-MnO_2	0	642.6	641.8	4.0	529.7	531.3	2.8
δ-MnO_2	6.4	642.5	641.8	8.3	529.6	531.3	5.5

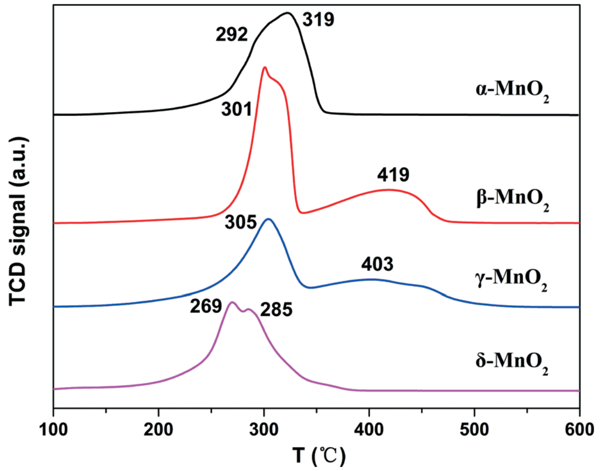

Fig. 6 H_2-TPR profiles of the α-, β-, γ- and δ-MnO$_2$ samples.

The reducibility tested by H_2-TPR could reflect the oxygen mobility in the samples: since δ-MnO$_2$ shows the reduction peak at the lowest temperature, it was proven to possess the most mobile oxygen species both at the surface and in the bulk among the four catalysts. Consequently, the high oxygen mobility causes more oxygen to be adsorbed and further excited to active oxygen, which would then be involved in the reaction.

3.6 XPS analysis

To identify the states of the surface Mn and O elements and check our deduction from the H_2-TPR experiment, XPS spectra were next measured. Fig. 7a shows the Mn $2p_{3/2}$ spectra of the series of catalysts. The peaks at 642.6 and 641.8 eV could be attributed to the surface Mn^{4+} and Mn^{3+}, respectively.[36,37] The Mn $2p_{3/2}$ peak of β-MnO$_2$ exhibited a certain shift of about 0.4 eV to a lower binding energy, (ESI,† Fig. S4). This shift could be regarded as a system shift because it also emerged at the O 1s peak (Fig. 7b). Thus, after the spectra were deconvoluted, the peaks of both Mn^{4+} and Mn^{3+} in β-MnO$_2$ shifted to lower binding energies by about 0.4 eV. A quantitative analysis on the Mn $2p_{3/2}$ spectra was performed and the surface element molar ratios of Mn^{4+}/Mn^{3+} are summarized in Table 2. Apparently, the surface Mn^{4+}/Mn^{3+} molar ratios of the catalysts were distinct in MnO$_2$ with different crystal structures. The δ-MnO$_2$ sample presented the highest Mn^{4+}/Mn^{3+} molar ratio (8.3). The sequence of surface Mn^{4+} percentage followed the order δ- > α- > γ- ≈ β-.

The XPS spectra of O 1s are shown in Fig. 7b. The asymmetrical O 1s spectra could be deconvoluted to two peaks. The main species at a binding energy of 529.7 eV was assigned to the lattice oxygen (O^{2-}) (denoted as O_{latt}),[37–39] and the signal at a binding energy of 531.3 corresponded to the surface adsorbed oxygen with low coordination (denoted as O_{ads})[37,40] such as O_2^{2-} or O^- belonging to defect-oxide or hydroxyl-like groups. Different from the other samples, the O 1s peaks of β-MnO$_2$ are shifted towards lower binding energies by about 0.4 eV, consistent with previous studies[30,41,42] and the results of the Mn 2p spectra. In view of the system shift by 0.4 eV on the spectra of β-MnO$_2$, the binding energy locations of both O_{ads} and O_{latt} in the β- sample are also disposed with a shift of about 0.4 eV when the deconvolution is carried out. The surface element molar ratios O_{latt}/O_{ads} were calculated and summarized in Table 2. They followed the sequence δ-MnO$_2$ (5.5) > α-MnO$_2$ (4.1) > γ-MnO$_2$ (2.8) > β-MnO$_2$ (2.4). Generally, oxidation reactions such as CO and NO oxidation on MnO$_x$ catalysts follow the Mars–van Krevelen mechanism,[43,44] implying that the lattice oxygen concentration could dominate the activity during the reaction.[45] Lee *et al.*[44] observed that MnO$_2$ with more lattice oxygen was more active than Mn$_2$O$_3$ for the oxidation of NO to NO$_2$. Tang *et al.*[26] have observed that the richer lattice oxygen in Mn–Ce composite catalysts were advantageous for the

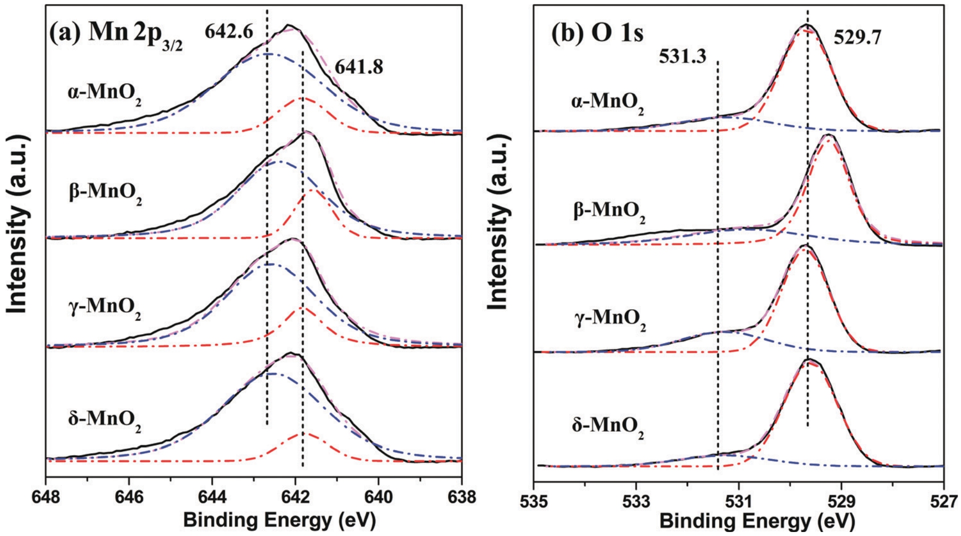

Fig. 7 XPS spectra of α-, β-, γ- and δ-MnO$_2$ samples: (a) Mn $2p_{3/2}$ and (b) O 1s.

HCHO oxidation. In this study, the surface molar ratios O_{latt}/O_{ads} followed the order of the catalytic activities for HCHO oxidation among the four types of MnO_2 catalyst, indicating that the activity is also closely related to the surface concentrations of O_{latt} species. Abundant lattice oxygen, such as that on δ-MnO_2, would lead to the excellent activity of MnO_2 catalysts for HCHO oxidation. However, this conclusion is just deduced from the XPS data, and to our knowledge, no previous report directly demonstrates the function of lattice oxygen in MnO_2 for HCHO catalytic oxidation. Furthermore, one recent study has claimed that the adsorbed oxygen species might play an important role in the total oxidation of toluene over MnO_2 catalysts.[46] Thus, the function of lattice oxygen needs to be verified by solid experimental data.

3.7 Lattice oxygen test

To confirm the role of lattice oxygen species on MnO_2 in this reaction, δ-MnO_2 was next tested in the absence of oxygen in reaction gases. The details about the pretreatment of catalyst are given in the experimental section. Fig. 8 shows the concentration of both HCHO and CO_2 as a function of time in the lattice oxygen test. After introducing HCHO into the reactor, CO_2 concentration first rapidly increased to a maximum and then descended gradually to a low level. HCHO was detected in outlet gas after about 20 min and then its concentration slowly increased to a high level. It is noted that the CO_2 concentration generated in the 75 °C test was much higher than that in the 50 °C test, showing that the active oxygen species in δ-MnO_2 was much more active at 75 °C than 50 °C. The ratio of consumption of oxygen to total oxygen in the δ-MnO_2 catalyst was stoichiometrically calculated based on the amount of CO_2 production. It is shown that 1.78% and 3.87% of the oxygen species were consumed during the 120 min reaction at 50 °C and 75 °C, respectively. After being purged by pure N_2 for 30 min at 150 °C, there would be exclusively surface adsorbed oxygen and lattice oxygen species left on the pretreated catalyst surface. However, as shown in Fig. 6, no peak corresponding to surface adsorbed oxygen species was observed in the H_2-TPR profile, indicating that the amount of surface adsorbed oxygen species should be at a considerably low level. As for the quantitative analysis, such a large amount of consumed oxygen during the reaction should mostly come from the lattice oxygen. Therefore, the high HCHO conversion rates in both tests would be attributed to the activated abounding surface lattice oxygen. The results confirmed that the lattice oxygen species were responsible for the total oxidation of HCHO over MnO_2 catalysts.

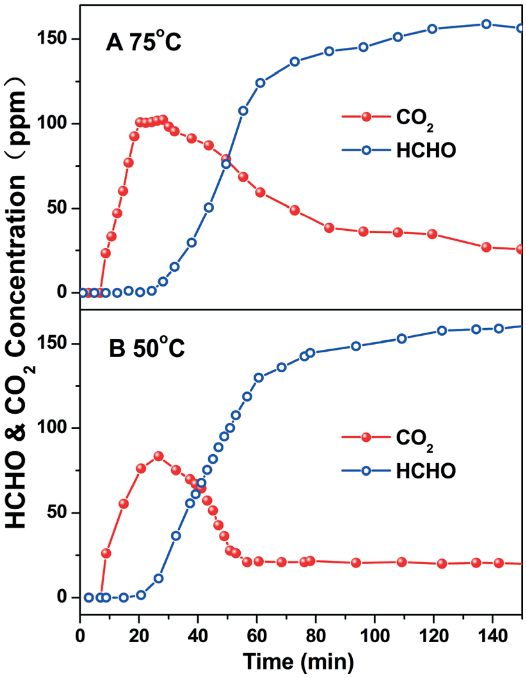

Fig. 8 Concentration variations of HCHO and CO_2 with reaction time in the lattice oxygen test.

Interestingly, the longer lasting production of CO_2 in the 75 °C test, especially the gradual reduction in the production rate from 60 minutes to 100 minutes, indicates that there might be lattice oxygen mobility from the bulk to the surface. After the surface lattice oxygen is partly consumed, the subsurface oxygen, even the more inner ones, gradually shift to the surface to participate in the oxidation reaction. As the mobility becomes lower upon moving from surface to bulk, the rate of supplementary oxygen species gradually decreases, thus leading to the drop in CO_2 production.

3.8 HCHO-TPD

To investigate the adsorption/desorption properties of HCHO on the surfaces of the MnO_2 catalysts, HCHO-TPD was next

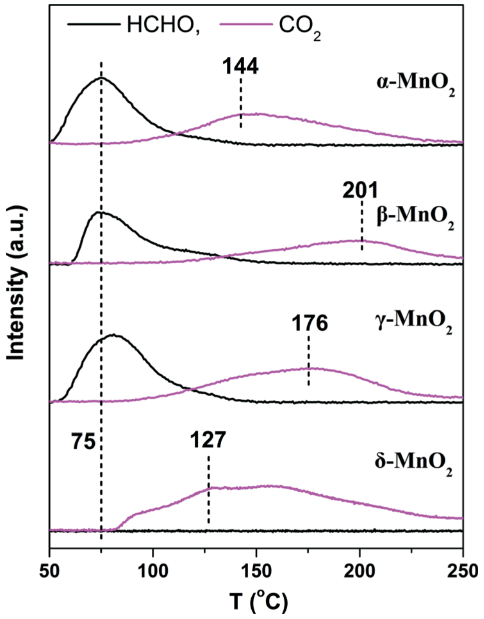

Fig. 9 HCHO-TPD results of α-, β-, γ- and δ-MnO_2 catalysts.

carried out. As shown in Fig. 9, the HCHO molecules were desorbed at around 50 °C and then reached their peaks at about 75 °C on the α-, β-, and γ-MnO_2 catalysts, while no HCHO desorption was observed on δ-MnO_2. CO_2 was detected on all samples during the HCHO-TPD starting at around 75 °C, with peaks at 144 °C, 201 °C, 176 °C and 127 °C, for the α–δ-MnO_2 catalysts respectively. CO_2-TPD experiments were also performed, and the results (ESI,† Fig. S5) show that the CO_2 desorption temperatures for the four catalysts were all lower than 100 °C, confirming that the CO_2 in the HCHO-TPD experiments was mainly produced by the oxidation of some adsorbed HCHO or intermediates.[47] Therefore, HCHO desorption and CO_2 production should be closely dependent on the activity of the surface lattice oxygen species. When the lattice oxygen species are highly active at low temperature, such as on the δ-MnO_2 catalyst, all adsorbed HCHO would be oxidized into CO_2 without desorption during the ramping temperature.

4. Conclusions

In summary, we prepared α-, β-, γ- and δ-type MnO_2 catalysts and observed their very different activities for the catalytic oxidation of HCHO. This enormous difference in activities originates from their different physical properties at the surface, K^+ content, tunnel structures, the mobility of oxygen species, lattice oxygen abundances and also HCHO adsorption/desorption properties. However, the tunnel structures and lattice oxygen mobility and abundances might play a more important role in the HCHO oxidation reaction. δ-MnO_2 has a special 2D layer tunnel structure and also contains the most active oxygen species and the highest amount of lattice oxygen species on the catalyst surface, therefore, presenting the highest activity of the four types of MnO_2 catalyst. Moreover, due to the high catalytic performance and facile preparation process, δ-MnO_2 may potentially be used as a support in applications of supported catalysts.

Acknowledgements

This work was financially supported by the National Natural Science Foundation of China (21422706) and the Program of the Ministry of Science and Technology of China (2012AA062702).

Notes and references

1 Y. Sekine, *Atmos. Environ.*, 2002, **36**, 5543.
2 J. Pei and J. Zhang, *HVAC&R Research*, 2011, **17**, 476.
3 R. Maddalena, M. Russell, D. Sullivan and M. Apte, *Environ. Sci. Technol.*, 2009, **43**, 5626.
4 J. Yang, Y. Qin, Y. Zeng and X. Ding, *Food Sci.*, 2014, **35**, 294.
5 J. Shie, C. Lee, C. Chiou, C. Chang, C. Chang and C. Chang, *J. Hazard. Mater.*, 2008, **155**, 164.
6 T. Noguchi and A. Fujishima, *Environ. Sci. Technol.*, 1998, **32**, 3831.
7 M. Chang and C. Lee, *Environ. Sci. Technol.*, 1995, **29**, 181.
8 C. Ma, X. Li and T. Zhu, *Carbon*, 2011, **49**, 2873.
9 C. Zhang, F. Liu, Y. Zhai, H. Ariga, N. Yi, Y. Liu, K. Asakura, M. Flytzani-Stephanopoulos and H. He, *Angew. Chem., Int. Ed.*, 2012, **51**, 9628.
10 B. Bai, H. Arandiyan and J. Li, *Appl. Catal., B*, 2013, **142**, 677.
11 C. Zhang, H. He and K. Tanaka, *Appl. Catal., B*, 2006, **65**, 37.
12 T. Quiroz, S. Royer, J. Bellat, J. Giraudon and J. Lamonier, *ChemSusChem*, 2013, **6**, 578.
13 C. Zhang and H. He, *Catal. Today*, 2007, **126**, 345.
14 B. Liu, Y. Liu, C. Li, W. Hu, P. Jing, Q. Wang and J. Zhang, *Appl. Catal., B*, 2012, **127**, 47.
15 B. Liu, C. Li, Y. Zhang, Y. Liu, W. Hu, Q. Wang, L. Han and J. Zhang, *Appl. Catal., B*, 2012, **111**, 467.
16 X. Tang, J. Chen, X. Huang, Y. Xu and W. Shen, *Appl. Catal., B*, 2008, **81**, 115.
17 H. Huang and D. Leung, *ACS Catal.*, 2011, **1**, 348.
18 C. Zhang, Y. Li, Y. Wang and H. He, *Environ. Sci. Technol.*, 2014, **48**, 5816.
19 C. Shi, B. Chen, X. Li, M. Crocker, Y. Wang and A. Zhu, *Chem. Eng. J.*, 2012, **200**, 729.
20 Z. Qu, S. Shen, D. Chen and Y. Wang, *J. Mol. Catal. A: Chem.*, 2012, **356**, 171.
21 Z. Huang, X. Gu, Q. Cao, P. Hu, J. Hao, J. Li and X. Tang, *Angew. Chem., Int. Ed.*, 2012, **51**, 4198.
22 Q. Wang, W. Jia, B. Liu, W. Zhao, C. Li, J. Zhang and G. Xu, *Chem. – Asian J.*, 2012, **7**, 2258.
23 L. Zhou, J. He, J. Zhang, Z. He, Y. Hu, C. Zhang and H. He, *J. Phys. Chem. C*, 2011, **115**, 16873.
24 L. Ma, D. Wang, J. Li, B. Bai, L. Fu and Y. Li, *Appl. Catal., B*, 2014, **148**, 36.
25 L. Nie, J. Yu, X. Li, B. Cheng, G. Liu and M. Jaroniec, *Environ. Sci. Technol.*, 2013, **47**, 2777.
26 X. Tang, Y. Li, X. Huang, Y. Xu, H. Zhu, J. Wang and W. Shen, *Appl. Catal., B*, 2006, **62**, 265.
27 H. Chen, J. H. C. Zhang and H. He, *J. Phys. Chem. C*, 2007, **111**, 18033.
28 T. Chen, H. Dou, X. Li, X. Tang, J. Li and J. Hao, *Microporous Mesoporous Mater.*, 2009, **122**, 270.
29 Y. Wang, A. Zhu, B. Chen, M. Crocker and C. Shi, *Catal. Commun.*, 2013, **36**, 52.
30 S. Liang, F. Bulgan, R. Zong and Y. Zhu, *J. Phys. Chem. C*, 2008, **112**, 5307.
31 S. Turner and P. Buseck, *Science*, 1979, **203**, 456.
32 Y. Chabre and J. Pannetier, *Prog. Solid State Chem.*, 1995, **23**, 1.
33 J. Post and D. Veblen, *Am. Mineral.*, 1990, **75**, 477.
34 J. Hou, L. Liu, Y. Li, M. Mao, H. Lv and X. Zhao, *Environ. Sci. Technol.*, 2013, **47**, 13730.
35 S. Devarajand and N. Munichandraiah, *J. Phys. Chem. C*, 2008, **112**, 4406.
36 A. Wollner, F. Lang, H. Schmelz and H. Knozinger, *Appl. Catal., A*, 1993, **94**, 181.
37 M. Toupin, T. Brousse and D. Belanger, *Chem. Mater.*, 2004, **16**, 3184.
38 S. Cai, D. Zhang, L. Zhang, L. Huang, H. Li, R. Gao, L. Shi and J. Zhang, *Catal. Sci. Technol.*, 2014, **4**, 93.

39 B. Tan, K. Klabunde and P. Sherwood, *J. Am. Chem. Soc.*, 1991, **113**, 855.

40 X. Tang, J. Chen, Y. Li, Y. Li, Y. Xu and W. Shen, *Chem. Eng. J.*, 2006, **118**, 119.

41 C. Yu, G. Li, L. Wei, Q. Fan, Q. Shu and J. Yu, *Catal. Today*, 2014, **224**, 154.

42 J. Li, C. Song and S. Liu, *Acta Chim. Sin.*, 2012, **70**, 2347.

43 R. Xu, X. Wang, D. Wang, K. Zhou and Y. Li, *J. Catal.*, 2006, **237**, 426.

44 S. Lee, K. Park, S. Kim, D. Kwon and S. Hong, *J. Air Waste Manage. Assoc.*, 2012, **62**, 1085.

45 W. Song and E. Hensen, *Catal. Sci. Technol.*, 2013, **3**, 3020.

46 F. Wang, H. Dai, J. Deng, G. Bai, K. Ji and Y. Liu, *Environ. Sci. Technol.*, 2012, **46**, 4034.

47 G. Busca, J. Lamotte, J. Lavalley and V. Lorenzelli, *J. Am. Chem. Soc.*, 1987, **109**, 5197.